



This is the accepted manuscript made available via CHORUS. The article has been published as:

Realization of a Hole-Doped Mott Insulator on a Triangular Silicon Lattice

Fangfei Ming, Steve Johnston, Daniel Mulugeta, Tyler S. Smith, Paolo Vilmercati, Geunseop Lee, Thomas A. Maier, Paul C. Snijders, and Hanno H. Weitering

Phys. Rev. Lett. **119**, 266802 — Published 27 December 2017

DOI: [10.1103/PhysRevLett.119.266802](https://doi.org/10.1103/PhysRevLett.119.266802)

Realization of a hole-doped Mott insulator on a triangular silicon lattice

Fangfei Ming,¹ Steve Johnston,¹ Daniel Mulugeta,¹ Tyler S. Smith,¹ Paolo Vilmercati,^{1,2} Geunseop Lee,³ Thomas A. Maier,⁴ Paul C. Snijders,^{5,1} and Hanno H. Weiering^{1,5}

¹*Department of Physics and Astronomy, The University of Tennessee, Knoxville, Tennessee 37996*

²*Joint Institute of Advanced Materials at The University of Tennessee, Knoxville, TN 37996*

³*Department of Physics, Inha University, Incheon 402-751, Korea*

⁴*Computational Science and Engineering Division and Center for Nanophase Materials Sciences, Oak Ridge National Laboratory, Oak Ridge, Tennessee 37831*

⁵*Materials Science and Technology Division, Oak Ridge National Laboratory, Oak Ridge, Tennessee 37831*

The physics of doped Mott insulators is at the heart of some of the most exotic physical phenomena in materials research including insulator-metal transitions, colossal magnetoresistance, and high-temperature superconductivity in layered perovskite compounds. Advances in this field would greatly benefit from the availability of new material systems with similar richness of physical phenomena, but with fewer chemical and structural complications in comparison to oxides. Using scanning tunneling microscopy and spectroscopy, we show that such a system can be realized on a silicon platform. Adsorption of one-third monolayer of Sn atoms on a Si(111) surface produces a triangular surface lattice with half-filled dangling bond orbitals. Modulation hole-doping of these dangling bonds unveils clear hallmarks of Mott physics, such as spectral weight transfer and the formation of quasi-particle states at the Fermi level, well-defined Fermi contour segments, and a sharp singularity in the density of states. These observations are remarkably similar to those made in complex oxide materials, including high-temperature superconductors, but highly extraordinary within the realm of conventional *sp*-bonded semiconductor materials. It suggests that exotic quantum matter phases can be realized and engineered on silicon-based materials platforms.

It has long been surmised that semiconductor surfaces could be ideal platforms for studying correlated electron phenomena in low-dimensional electron systems [1-8]. In particular, the reduced coordination of the surface atoms of covalently bonded semiconductors implies the existence of a two-dimensional (2D) periodic array of partially filled dangling bonds. Most of these systems are susceptible to band Jahn-Teller or charge ordering instabilities, however, which can lead to a complete restructuring of the surface [9]. From a chemical perspective, these types of instabilities are driven by the system's tendency to saturate or

eliminate partially filled dangling bonds through orbital rehybridization and/or the formation of new bonds. From the physics perspective, these 2D systems undergo spontaneous symmetry breaking transitions that are driven by strong electron-phonon coupling, wiping out most or all density of states (DOS) near the Fermi level E_F . In principle, the charge ordering instability competes with magnetic or superconducting instabilities, although this type of physics seems mostly limited to the realm of transition metal oxides with narrow d -bands and moderate-to-strong electron correlations [10]. The beauty of those systems is that the various interactions and resulting order parameters can be tuned via e.g. controlled doping experiments, providing access to important quantum matter phases, including unconventional superconductivity [10].

The ‘ α -phases’ of Sn and Pb on Si(111) or Ge(111) are believed to exhibit similarly rich physics [3, 4, 6-8, 11, 12]. These phases are formed by adsorbing a $1/3$ monolayer (ML) of Sn or Pb on the Si(111) or Ge(111) surface in an ordered $(\sqrt{3}\times\sqrt{3})R30^\circ$ arrangement. In this geometry, the substrate’s dangling bonds are passivated while each Sn or Pb adatom contributes one half-filled dangling bond per unit cell (see Fig. 1(a)). With the exception of Sn on Si(111), these systems all undergo a charge ordering transition at low temperature [3, 4, 8, 12]. A recent angle-resolved photoemission (ARPES) study indicated that Sn on Si(111) is an antiferromagnetic Mott insulator below 200 K [13], or perhaps a magnetic band or Slater insulator [14]. If the Mott scenario can be confirmed, Sn on Si(111) (henceforth $\sqrt{3}$ -Sn), would represent one of the closest experimental realizations of the spin $1/2$ triangular-lattice antiferromagnetic Heisenberg model. Such a system could host exotic spin states, such as a chiral spin state or a quantum spin liquid [15], and become superconducting with doping [7].

A critical first step toward accomplishing this goal would be the successful introduction of excess charges into the $\sqrt{3}$ -Sn dangling bond lattice without introducing structural and/or chemical disorder. Here, we employ a modulation doping scheme by using Si(111) substrates with various bulk doping levels [16]. Because the charge reservoir in the dangling bond surface state is in thermodynamic equilibrium with that of the doped bulk material, the use of heavily-doped p-type (n-type) substrates should in principle produce a hole-doped (electron-doped) surface layer (see Note 1 in Ref. [17]). We used n-type silicon substrates with room temperature (RT) resistivities of 0.002, 0.03, and 3 $\Omega\cdot\text{cm}$, and p-type (B-doped) substrates with RT resistivities of 0.03, 0.008, 0.004 and 0.001 $\Omega\cdot\text{cm}$. They are labeled according to their doping type and resistivity, for instance “n-0.002” or “p-0.008” (smaller numbers represent higher bulk doping levels). The substrate with the largest boron content, p-0.001, is labeled $B\sqrt{3}$. Here, segregated boron atoms form a $(\sqrt{3}\times\sqrt{3})R30^\circ$ superstructure below the topmost Si layer, which corresponds to the highest achievable doping level with our modulation doping approach [16].

The silicon substrates were annealed to temperatures over 1000 $^\circ\text{C}$ in ultrahigh vacuum (UHV) so as to prepare atomically clean Si(111) 7×7 and Si(111) $(\sqrt{3}\times\sqrt{3})R30^\circ$ -B substrates for the growth of the $\sqrt{3}$ -Sn structure. Sn atoms were deposited from a thermal effusion cell while keeping the substrate temperature at 550 $^\circ\text{C}$, which resulted in the formation of a well-ordered $\sqrt{3}$ -Sn structure. An Omicron low-temperature scanning tunneling microscope (STM) was used

for atomic resolution imaging and spectroscopy of the (un)doped $\sqrt{3}$ -Sn surfaces. Additional details can be found in the supplementary text [17].

Using the modulation doping scheme, we were able to hole-dope the $\sqrt{3}$ -Sn structure up to about 10%. We were unable to create an electron-doped $\sqrt{3}$ -Sn structure on the n-type substrates, however. This difficulty is related to the fact that high-temperature annealing in UHV leads to dopant conversion in the subsurface region of n-type Si [18-20]. To check this scenario for our samples, we performed current-voltage ($I(V)$) measurements on the n-type substrate with the STM. Our data confirm the existence of a p-type inversion layer below the surface of the n-3 sample (see Note 2 in Ref. [17]), indicating that its surface is hole doped. The subsurface layer of n-0.03 and n-0.002 sample is partially compensated but remains n-type.

Fig. 1(b) shows a STM topographic image of the $\sqrt{3}$ -Sn surface. The atoms seen in this image are the Sn adatoms forming a $(\sqrt{3}\times\sqrt{3})R30^\circ$ superstructure relative to the underlying Si(111) substrate [4], (Fig. 1(a)). The image remains the same, regardless of the doping level or doping type, except for the fact that the $\sqrt{3}$ -Sn domain size decreases with increased hole doping (see Note 3 in Ref. [17]). We find no evidence for structural distortions in these images.

Fig. 2(a) shows a series of dI/dV tunneling spectra, recorded at 77 K, representing the local density of states (LDOS) of the $\sqrt{3}$ -Sn surface for different doping levels [22]. The bottommost n-0.002 spectrum agrees well with the spectrum expected for an undoped Mott-Hubbard insulator [6,7] with a lower and an upper Hubbard band (LHB/UHB) centered at about -0.4 V and +0.5 V, respectively, and a 0.2 eV Mott gap in between. This assignment is fully consistent with previous experiments [6,13,23] and theoretical calculations [11,13,24]. The Mott insulating nature of the n-0.002 sample indicates that the excess electrons from the partially compensated substrate are trapped by localized defect states (see Note 2 in Ref. [17]).

By switching to the n-0.03 substrate, the system enters the hole-doped regime. This hole doping is signaled by the formation of a shoulder slightly above E_F , which evolves into a quasi-particle peak (QPP) whose tail crosses the Fermi level as more holes are added to the surface. Note that the QPP is already visible for the n-3 substrate, consistent with the established presence of the p-type inversion layer below the surface. It is centered at about + 0.1 eV and its intensity is greatest for the $B\sqrt{3}$ -Sn surface. The origin of this peak must be electronic in nature. It cannot be associated with a structural distortion as the STM images of the doped and undoped systems are identical. While hole doping clearly metallizes the $\sqrt{3}$ -Sn surface, the zero bias conductance in STM remains suppressed for all doping levels, except for the $B\sqrt{3}$ -Sn case (see Note 4 in Ref. [17]). This is reminiscent of the pseudo-gap feature observed on lightly doped cuprate and iridate compounds [25, 26]. However, unlike the cuprates and iridates, the spectral features of the $\sqrt{3}$ -Sn system are remarkably uniform spatially. Fig. 2(b) shows an STM image of the $B\sqrt{3}$ -Sn surface, along with a series of tunneling spectra recorded at regular intervals across the $B\sqrt{3}$ -Sn domain. The latter is structurally uniform and there is only very minor variation in the position and intensity of the low-energy spectral features

(UHB/LHB/QPP). In contrast, doped cuprate and iridate materials usually exhibit competing nanophases such as striped or checkerboard-like charge ordered regions [27]. This suggests that these competing orders are material-specific and are not intrinsic to the single-band Hubbard model.

It is evident from Fig. 2(a) that the growth of the QPP with hole-doping is accompanied by a reduction of spectral weight of the Hubbard bands. The spectral weights can be estimated by integrating the areas under the UHB, LHB and QPP for each doping level, keeping in mind that the total spectral weight should be independent of doping. This procedure is described in detail in Supplementary Note 5 in Ref. [17] and the result is shown in Fig. 2(c). The spectral weight of the QPP reaches a maximum of about 20% on the $\text{B}\sqrt{3}\text{-Sn}$ sample, which corresponds to a hole doping level of about 10% [17]. The observed spectral weight transfer is a very distinctive hallmark of Mott physics [28, 29], and is well reproduced by our Dynamical Cluster Approximation (DCA) calculations [30], shown in Fig. 2(d), where we used the hopping parameters and Hubbard U from Ref. [13]. Importantly, the observed spectral weight transfer rules out the recently proposed Slater insulator scenario for the undoped system [14], where the band gap arises from magnetic ordering and associated band folding. Doping a Slater band insulator would result in a repositioning of the chemical potential and/or collapse of the gap with vanishing magnetization, but does not lead to a transfer of spectral weight from the high-energy spectral features (UHB/LHB) to a new quasi particle state inside the gap [29].

At high hole doping levels, quasi-particles contributing to the spectral weight near E_F should acquire momentum dispersion and develop a well-defined Fermi surface contour. The Fermi contour can be acquired by measuring the quasi-particle interference (QPI) patterns in dI/dV STM imaging near zero bias [31]. These experiments are necessarily limited to low temperature and, consequently, to only the most conductive samples. Fig. 3(a) shows a topographic STM image of the $\text{B}\sqrt{3}\text{-Sn}$ system, acquired with a tunneling bias of - 5 mV at 4.4 K. The Sn adatoms are perfectly equivalent in both filled and empty state imaging, again ruling out the presence of a charge-density modulation [3] or structural rippling at 4.4 K. Fig. 3(b) is the simultaneously acquired dI/dV image. The latter reveals a significant spatial modulation of the differential tunneling conductance $g(\mathbf{r}, V) = dI(\mathbf{r}, V) / dV$ as quasi-particles scatter at defects and, consequently, between different \mathbf{k} -points on the constant energy contour $\mathbf{k}(E=eV)$. Its Fourier transform, $g(\mathbf{q}, V)$, shown in Fig 3(d), represents the power spectrum of the density modulation in Fig. 3(b). Note that for zero bias, the scattering vector $\mathbf{q} = 2\mathbf{k}_F \pm \mathbf{G}$, where \mathbf{G} is a reciprocal lattice vector of the $(\sqrt{3}\times\sqrt{3})R30^\circ$ superstructure (see Note 6 in Ref. [17]), meaning that the Fermi surface can be reconstructed from the QPI Fourier transform [31].

Filled-state $g(\mathbf{q}, V)$ maps are shown in Figs. 3(c) and 3(d); empty state maps are shown in Figs. 3(e) and 3(f). The most intense spots are the Bragg peaks of the $(\sqrt{3}\times\sqrt{3})R30^\circ$ surface structure, which allows us to determine the magnitude and direction of the scattering vectors. It should be noted that the clarity of the scattering features in these maps is extraordinary, which is true even for the raw data (see Fig. S7 in Ref. [17]). The differential conductance maps

furthermore reveal the presence of approximately equilateral triangles pointing toward the origin. They are highlighted in green. The outer edges of these triangles form a warped hexagonal constant energy contour, highlighted in red. The other edges are scattering replicas involving a reciprocal lattice vector translation. The triangles gradually shrink going from negative to positive bias, meaning that the corresponding scattering vectors disperse with energy. The dispersion relation $q(E)$ is plotted along the $\overline{\Gamma K}$ and $\overline{\Gamma M}$ directions of the surface Brillouin zone in Figs. 3(k) and 3(l), respectively.

We simulated the $g(\mathbf{q}, V)$ maps using a single-band model obtained from density functional theory (DFT) calculations [13] and the T-Matrix formalism, assuming a single point-like potential scatterer (see [32] and Note 7 in Ref. [17]). The resulting simulated maps are shown in Figs. 3(g-j), alongside the corresponding experimental maps. Both the triangular features (green) and warped contours (red) are well reproduced. The experimental and theoretical dispersion relations in Figs. 3(k) and 3(l) are also very similar. The warping of the triangular features in the simulated power spectrum can be traced to the warped hexagonal shape of the Fermi contour, as seen in DFT calculations [13, 4]. The experimental triangles have flatter sides, however, which is particularly evident in panels 3(f) and 3(j): the constant energy contour at +10 meV appears perfectly nested. This flattening of the constant energy contours as compared to the DFT results reflects the renormalization of the quasi-particle dispersion due to the Hubbard interaction. Most importantly, the existence of a Fermi surface contour in the hole-doped system that is reminiscent of the non-interacting bands of the $\sqrt{3}$ -Sn structure, is conclusive evidence that the origin of the QPP should be attributed to the spectral weight transfer of a hole-doped Mott insulator. Clearly, the QPP feature is intrinsic to the $\sqrt{3}$ -Sn structure and cannot be related to the formation of some impurity band, which should have a completely different dispersion, if any.

Closer inspection of the QPP offers a preview of what might happen if the hole-doping level could be pushed beyond the ten percent level achieved for the $B\sqrt{3}$ -Sn surface. The inset of Fig. 4 shows the recognizable QPP just above zero bias in dI/dV spectrum; this time the spectrum is recorded at 4.4 K. Note the very sharp spike on top of the QPP. The zoomed-in spectra in Fig. 4 clearly reveal the emergence of a singularity in the DOS ~ 6 meV below the Fermi level, which is becoming increasingly prominent as the temperature decreases. This feature can be attributed to a van Hove singularity in the DOS [33], associated with the saddle point in the quasi-particle band dispersion near the \overline{M} -point [13]. Indeed, the experimental and theoretical dispersions in Fig. 3(l) exhibit a kink near the M-point at about -5 meV, consistent with this saddle point. Further hole doping is expected to drive the singularity up to the Fermi level, which almost certainly would give rise to an electronic instability. In fact, such an instability may already exist below the current measurement temperature minimum of 4.4 K.

In light of the strong on-site Coulomb repulsion and approximate nesting conditions, one could envision two types of instability. The first would be similar to that envisioned for e.g. heavily doped graphene [34]. With its hexagonal Fermi contour and saddle points at the \overline{M} -

points, graphene would be susceptible to a *d*-wave superconducting instability if only the van Hove singularity at ~ 2 eV [35] from the Dirac point could be driven to the vicinity of Fermi level, as it is here. Likewise, both doped Mott physics and nesting have been considered essential for *d*-wave pairing in high temperature superconductors [36, 37]. The alternative scenario would be a competing charge-order or spin-density wave instability. Charge ordering in related systems nucleates at defects sites [38] for which there is no evidence here. On the other hand, the near perfect nesting conditions with three 120° rotated nesting vectors could give rise to a non-coplanar chiral spin order [39]. While the system would not exhibit long-range magnetic order, chirality would exist at finite temperatures, producing a spontaneous quantum Hall effect [39]. More doping studies will be needed to determine if these scenarios can indeed be realized on the silicon platform.

Acknowledgement: This work was primarily funded by the National Science Foundation under grant DMR 1410265. S.J. is partially funded by the University of Tennessee's Science Alliance Joint Directed Research and Development (JDRD) program, a collaboration with Oak Ridge National Laboratory. T.M. was sponsored by the Laboratory Directed Research and Development Program of Oak Ridge National Laboratory, managed by UT-Battelle, LLC, for the U. S. Department of Energy. G.L. acknowledges supports from the National Research Foundation of Korea (NRF) funded by the Korean government (MSIP) (NRF-2017R1A2B2003928).

References

1. J. E. Northrup, J. Ihm, and M. L. Cohen, Phys. Rev. Lett. **47**, 1910 (1981).
2. J. Ortega, F. Flores, and A. Levy Yeyati, Phys. Rev. B **58**, 4584 (1998).
3. J. M. Carpinelli, H. H. Weitering, E. W. Plummer, and R. Stumpf, Nature **381**, 398 (1996).
4. J. M. Carpinelli, H. H. Weitering, M. Bartkowiak, R. Stumpf, and E. W. Plummer, Phys. Rev. Lett. **79**, 2859 (1997).
5. H. H. Weitering, X. Shi, P. D. Johnson, J. Chen, N. J. DiNardo, and K. Kempa, Phys. Rev. Lett. **78**, 1331 (1997).
6. S. Modesti, L. Petaccia, G. Ceballos, I. Vobornik, G. Panaccione, G. Rossi, L. Ottaviano, R. Larciprete, S. Lizzit, and A. Goldoni, Phys. Rev. Lett. **98**, 126401 (2007).
7. G. Profeta, and E. Tosatti, Phys. Rev. Lett. **98**, 086401 (2007).
8. R. Cortés, A. Tejada, J. Lobo-Checa, C. Didiot, B. Kierren, D. Malterre, J. Merino, F. Flores, E. G. Michel, and A. Mascaraque, Phys. Rev. B **88**, 125113 (2013).

9. C. B. Duke, Chem. Rev. **96**, 1237-1260 (1996).
10. J. Orenstein, and A. J. Millis, Science **288**, 468-474 (2000).
11. P. Hansmann, T. Ayrat, L. Vaugier, P. Werner, and S. Biermann, Phys. Rev. Lett. **110**, 166401 (2013).
12. J. Avila, A. Mascaraque, E. G. Michel, M. C. Asensio, G. LeLay, J. Ortega, R. Pérez, and F. Flores, Phys. Rev. Lett. **82**, 442 (1999).
13. G. Li, P. Höpfner, J. Schäfer, C. Blumenstein, S. Meyer, A. Bostwick, E. Rotenberg, R. Claessen, and W. Hanke, Nat. Commun. **4**, 1620 (2013).
14. J. H. Lee, X. Y. Ren, Y. Jia, and J. H. Cho, Phys. Rev. B **90**, 125439 (2014).
15. P. Fazekas, and P. W. Anderson, Philos. Mag. **30**, 423 (1974).
16. F. Ming, D. Mulugeta, W. Tu, T. S. Smith, P. Vilmercati, G. Lee, Y. T. Huang, R. D. Diehl, P. C. Snijders, and H. H. Weitering, Nat. Commun. **8**, 14721 (2017).
17. See Supplemental Material at [URL will be inserted by publisher] for [band alignment measurement; spectral weight transfer estimation; sample growth and surface morphology; temperature dependent Mott transitions; spatial homogeneity; processing procedure of the QPI data; details about theoretical calculations], which includes Refs. [6,13,30,18-20,40-51].
18. M. Liehr, M. Renier, R. A. Wachnik, and G. S. Scilla, J. Appl. Phys. **61**, 4619-4625 (1987).
19. S. Bensalah, J-P. Lacharme, and C. A. Sébenne, Phys. Rev. B **43** 14441 (1991).
20. J. D. Mottram, A. Thanailakis, and D. C. Northrop, J. Phys. D **8**, 1316 (1975).
21. M. Rashidi, M. Taucer, I. Ozfidan, E. Lloyd, M. Koleini, H. Labidi, J. L. Pitters, J. Maciejko, and R. A. Wolkow, Phys. Rev. Lett. **117**, 276805 (2016).
22. J. Tersoff, & D. R. Hamann, Phys. Rev. Lett. **50**, 1998 (1983).
23. A. Charrier, R. Pérez, F. Thibaudau, J. M. Debever, J. Ortega, F. Flores, and J. M. Themlin, Phys. Rev. B **64**, 115407 (2001).
24. S. Schuwalow, D. Grieger, and F. Lechermann. Phys. Rev. B **82**, 035116 (2010).
25. P. Cai, W. Ruan, Y. Peng, C. Ye, X. Li, Z. Hao, X. Zhou, D.-H. Lee, and Y. Wang, Nat. Phys. **12**, 1047 (2016).
26. I. Battisti, K. M. Bastiaans, V. Fedoseev, A. De La Torre, N. Iliopoulos, A. Tamai, E. C. Hunter, R. S. Perry, J. Zaanen, F. Baumberger and M. P. Allan, Nat. Phys. **13**, 21 (2017).
27. P. A. Lee, N. Nagaosa, and X. G. Wen, Rev. Mod. Phys. **78**, 17 (2006).
28. E. Louis, F. Flores, F. Guinea, and J. Tejedor, J. Phys. C **16**, L39 (1983).
29. H. Eskes, , M. B. J. Meinders, G. A. Sawatzky, Phys. Rev. Lett. **67**, 1035 (1991).
30. T. Maier, M. Jarrell, T. Pruschke, M. H. Hettler, Rev. Mod. Phys. **77**, 1027 (2005).
31. L. Petersen, P. Hofmann, E. W. Plummer, and F. Besenbacher, J. Electron. Spectrosc. Relat. Phenom. **109**, 97-115 (2000).
32. H. Alloul, J. Bobroff, M. Gabay, and P. J. Hirschfeld, Rev. Mod. Phys. **81**, 45 (2009).
33. A. Piriou, N. Jenkins, C. Berthod, I. Maggio-Aprile, and Ø. Fischer, Nat. Commun. **2**, 221 (2011).
34. R. Nandkishore, L. S. Levitov, and A. V. Chubukov, Nat. Phys. **8**, 158-163 (2012).
35. R. Saito, G. Dresselhaus, and M. S. Dresselhaus, *Physical Properties of Carbon Nanotubes*

- (Imperial College Press, London, 1998).
36. R. S. Markiewicz, J. Phys. Chem. Solids **58**, 1179-1310. (1997).
 37. D. M. Newns, C. C. Tsuei, and P. C. Pattnaik, Phys. Rev. B **52**, 13611 (1995).
 38. H. H. Weitering, J. M. Carpinelli, A. V. Melechko, J. Zhang, M. Bartkowiak, and E. W. Plummer, Science **285**, 2107-2110 (1999).
 39. I. Martin, and C. D. Batista, Phys. Rev. Lett. **101**, 156402. (2008).
 40. S.M. Sze, *Physics of Semiconductor Devices Ed. 3* (John Wiley & Sons, 1981).
 41. F. J. Himpsel, G. Hollinger, and R. A. Pollak, Phys. Rev. B **28**, 7014 (1983).
 42. W. Mönch, *Semiconductor surfaces and interfaces* (Springer Science & Business Media, 2013).
 43. H. Zheng, J. Kroger, and R. Berndt, Phys. Rev. Lett. **108**, 076801 (2012).
 44. V. W. Brar et al. Nat. Phys. **7**, 43 (2010).
 45. F. Marczinowski, J. Wiebe, F. Meier, K. Hashimoto, and R. Wiesendanger, Phys. Rev. B **77**, 115318 (2008).
 46. C. Törnevik, M. Hammar, N. G. Nilsson, and S. A. Flodström, Phys. Rev. B **44**, 13144-13147 (1991).
 47. R. M. Feenstra, J. A. Stroscio, and A. P. Fein, Surf. Sci. **181**, 295-306 (1987).
 48. P. Martensson, R. M. Feenstra, Phys. Rev. B **39**, 7744-7753 (1989).
 49. M. B. J. Meinders, H. Eskes and G. A. Sawatzky, Phys. Rev. B **48**, 3916 (1993).
 50. M. P. Allan, A. W. Rost, A. P. Mackenzie, Yang Xie, J. C. Davis, K. Kihou, C. H. Lee, A. Iyo, H. Eisaki, and T.-M. Chuang, Science **336**, 563-567 (2012).
 51. S. Grothe, S. Johnston, S. Chi, P. Dosanjh, S. A. Burke, and Y. Pennec, Phys. Rev. Lett. **111**, 246804 (2013).

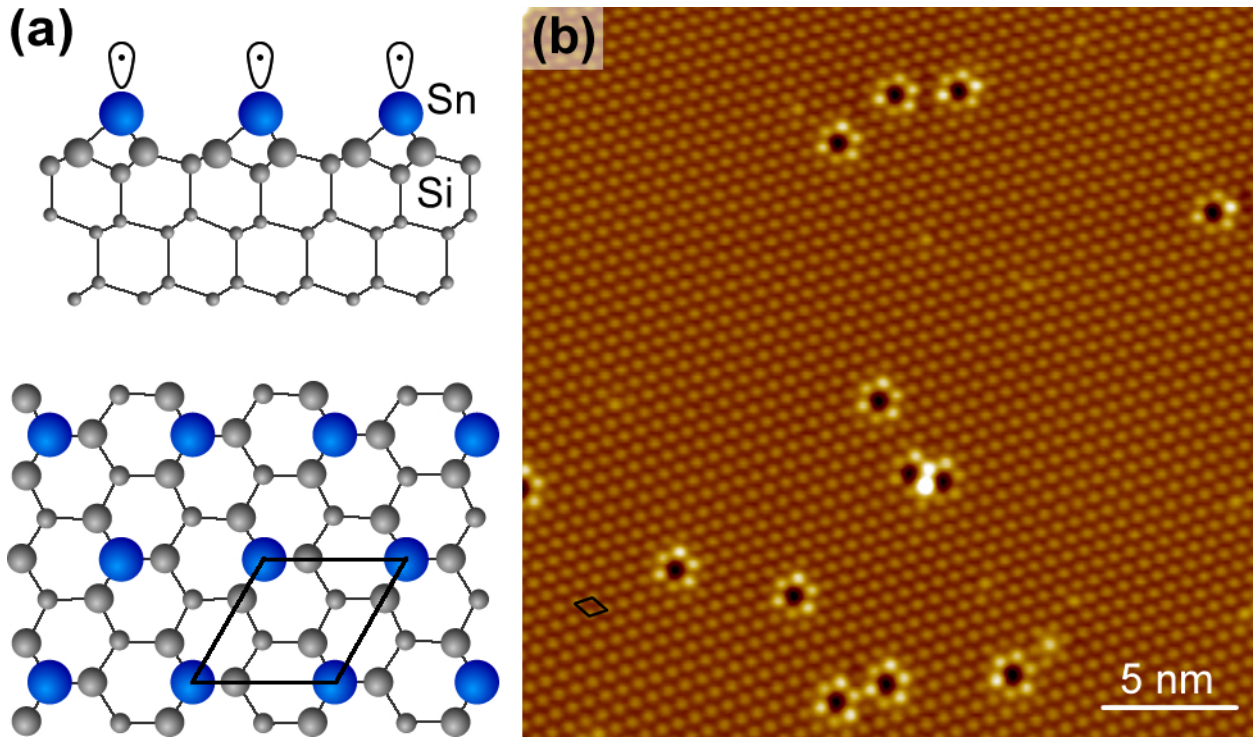


FIG. 1 Structure and STM topography of the $\sqrt{3}$ -Sn Mott insulating phase of Sn on Si(111). (a) Side view (top) and top view (bottom) of the $\sqrt{3}$ -Sn structure. The Sn adatoms are colored in blue, each contributing a nominally half-filled dangling bond orbital. There are no other dangling bonds present in this structure. (b) STM image of the $\sqrt{3}$ -Sn structure on a n-0.002 Si(111) substrate, recorded at 77 K ($V_s = -2$ V, $I_t = 0.1$ nA). The individual Sn atoms are clearly resolved. Dark features surrounded by hexagonal rings of bright adatoms likely correspond to substitutional Si defects in the Sn layer. Diamonds in panels (a) and (b) mark the $(\sqrt{3} \times \sqrt{3})R30^\circ$ unit cell.

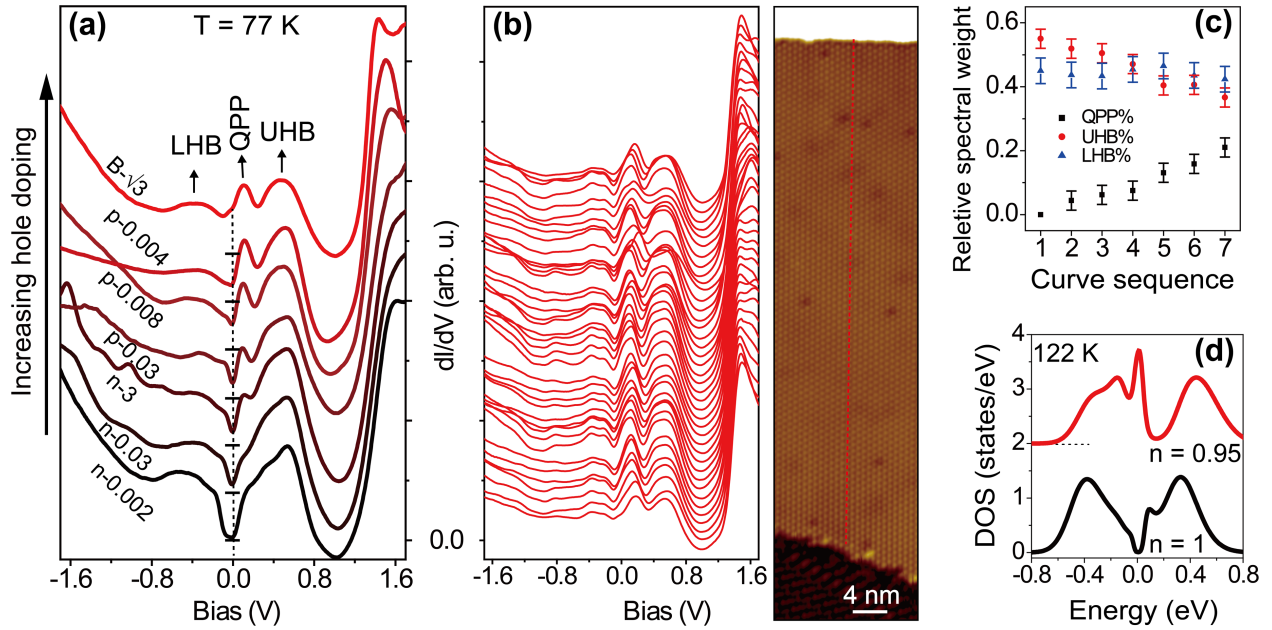


FIG. 2 (a) dI/dV spectra (\propto LDOS) measured at 77 K for the $\sqrt{3}$ -Sn surface grown on various n-type and p-type Si substrates. The spectra are normalized to a bulk feature at 1.6 V. Horizontal tick marks on the dashed vertical line at zero bias indicate the origin of the differential conductance axis for each curve. Note the negative differential resistance between 0.8 eV and 1.2 eV, consistent with other tunneling spectroscopy studies of localized dangling bond states [21]. (b) dI/dV spectra recorded at 5 K (left) along a line spanning a wide terrace of the $B\sqrt{3}$ -Sn phase (right). The terrace is bound by two step edges. The spectra show that the intensity and location of the low energy spectral features (± 0.7 V, UHB, LHB, QPP) are constant across the surface. One spectrum is recorded for every other unit cell. (c) Relative intensities of the UHB, LHB and QPP according to the spectral integration procedure in Supplementary Note 5 [17]. (d) Density of states obtained from DCA calculations for the undoped and five-percent hole-doped $\sqrt{3}$ -Sn surfaces at 122 K. The spectra in (a), (b) and (d) are offset vertically for clarity.

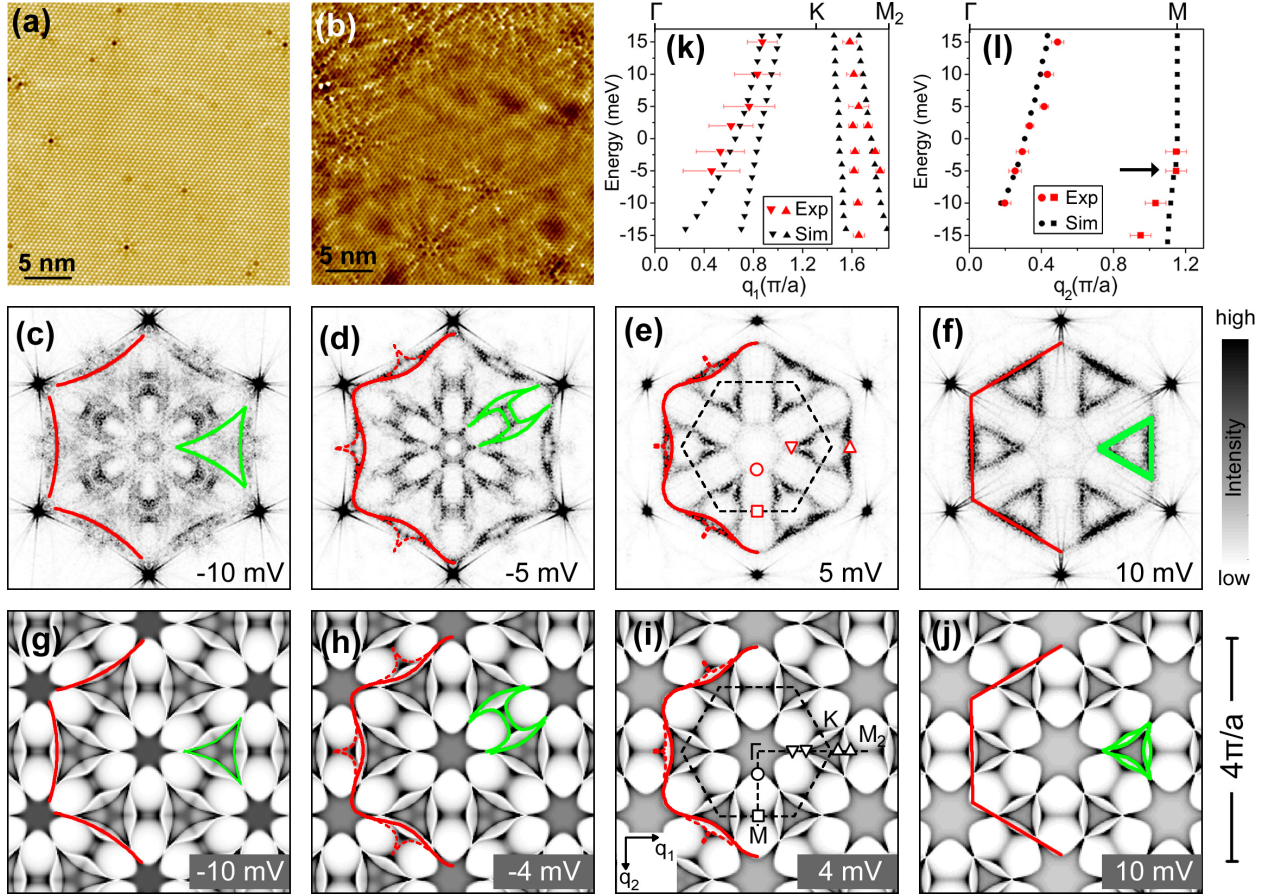


FIG. 3 Quasi particle interference patterns of the hole doped $\sqrt{3}$ -Sn Mott insulator on the $B\sqrt{3}$ substrate. (a) STM topographic image and (b) simultaneously acquired differential conductance map $g(\mathbf{r}, V)$ at -5 mV and 4.4 K. (c-f), Fourier transforms $g(\mathbf{q}, V)$ of the conductance maps $g(\mathbf{r}, V)$ acquired at different voltages. Note that panel (d) is the Fourier transform of image (b). The $g(\mathbf{q}, V)$ images have been rotated such that a $\overline{\Gamma K}$ direction runs horizontally while a $\overline{\Gamma M}$ direction runs vertically, as indicated in panels (e) and (i). The $g(\mathbf{q}, V)$ images were symmetrized, employing the three-fold rotational lattice symmetry in conjunction with the mirror symmetry in k-space (see Fig. S7 in Ref. [17]). The six outer spots are the Bragg spots of the $(\sqrt{3}\times\sqrt{3})R30^\circ$ real space lattice. (g-j) Simulated $g(\mathbf{q}, V)$ using the non-interacting band structure from Ref. [13] and applying the standard T-Matrix formalism for a single scattering defect [23]. Note the warped hexagonal contour in the experimental and theoretical power spectra, indicated in red. This is the $|\mathbf{q}|=2|\mathbf{K}(E)|$ contour, where $\mathbf{K}(E)$ is a constant energy contour in the surface state band structure. (k&l) Dispersion relation $E(\mathbf{q})$ extracted from the bias dependent $g(\mathbf{q}, V)$ images along the $\overline{\Gamma K M_2}$ direction (k) and $\overline{\Gamma M}$ direction (l). Red symbols represent the experimental data points (see Fig. S8 in Ref. [17]). Black dots are the theoretical results. The kink (labelled with an arrow in (l)) in the band dispersion near the M-point at -6 meV is consistent with the presence of the van Hove singularity in Fig. 4.

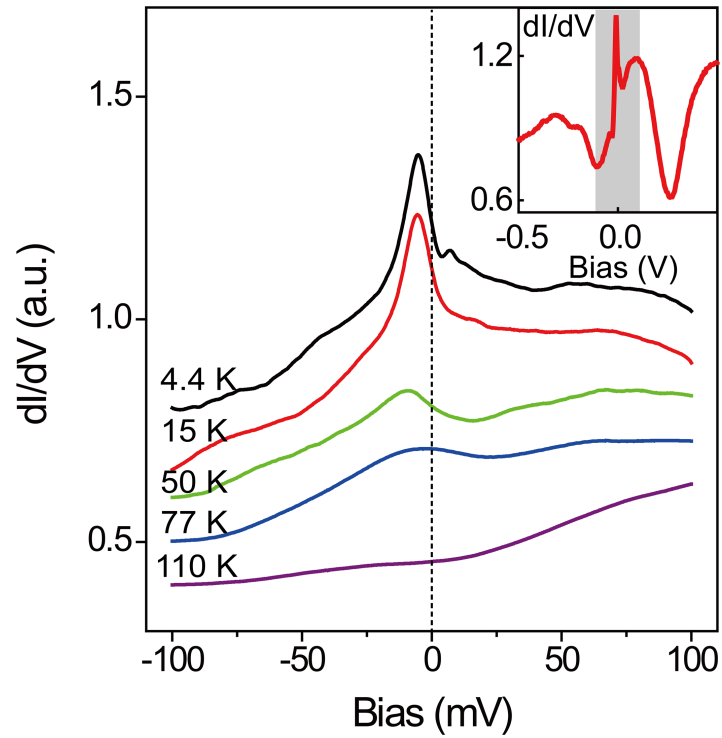


FIG. 4 Temperature dependent dI/dV spectra of the $\text{Bi}\sqrt{3}\text{-Sn}$ surface, showing an emerging van Hove singularity at about 6 mV below the Fermi level. The inset in panel (d) shows the 4.4 K spectrum on a larger bias scale. On this scale, the van Hove singularity is visible as a sharp spike riding on top of the QPP. The bias range displayed in the main panel is marked in gray.